

# Active CMOS Array Sensor for Time-Resolved Fluorescence Detection

George Patounakis, *Member, IEEE*, Kenneth L. Shepard, *Senior Member, IEEE*, and Rastislav Levicky

**Abstract**—Surface-based sensing assays based on fluorescence-based detection have become commonplace for both environmental and biomedical diagnostics. Traditional array scanners are expensive, large, and complex instruments. This paper describes the design of an active CMOS biosensor substrate for fluorescence-based assays that enables time-gated, time-resolved fluorescence spectroscopy without the need for an external reader. The array is sensitive to photon densities as low as  $1.15 \times 10^8/\text{cm}^2$ , has a dynamic range of over 74 dB, and has subnanosecond timing resolution. Sensitivity is achieved through subsampling and averaging.

**Index Terms**—Biochips, biosensor, CMOS imager, fluorescence spectroscopy, microarray.

## I. INTRODUCTION

**S**URFACE-BASED sensing assays have become commonplace for both environmental and biomedical diagnostics [1]–[3]. Analyte “targets” from solution bind to appropriate “probe” molecules immobilized on a solid support, generally a passive glass substrate, as a result of strong and specific probe–target interactions. Multiplexed detection occurs by constructing an array of different probes on the surface. For DNA analysis, high-density microarrays examine gene expression at the scale of entire genomes by simultaneously assaying target mixtures derived from expressed mRNA against thousands of array sites (locations), each bearing probes for a specific gene [3]. Microarrays generally quantify target concentrations in relative terms, e.g., in the form of a ratio to hybridization signal obtained using a “reference” target sample. Other biosensing applications are calibrated to provide absolute target concentrations.

Fluorescent-based detection, in which the target is labelled with a fluorophore, has arguably become the standard for quantifying the extents of probe–target binding in surface-based sensing assays [4]. Traditional microarray scanners consist of an excitation source (usually a laser) with the fluorescent light emitted by bound target fluorophores focused and collected, through a generally lossy optical path, onto a cooled charge-coupled device (CCD) or photomultiplier tube (PMT). Optical filtering is used to improve the SNR by removing

“background” light or reflected excitation light. Generally, arrays must be sensitive to fluorophore concentrations from  $10^8$  to  $10^{11} \text{ cm}^{-2}$ .

Fluorophores have associated with them a characteristic lifetime, which defines the exponential fluorescent decay transient after the removal of the excitation source. These lifetimes, on the order of nanoseconds for organic dyes, are characteristic of the dye and its environment and can be used in addition to color and intensity for multiplexed detection. Quantum-dot fluorophores can have lifetimes exceeding 15 ns at the cost of slightly lower quantum yields [5]. Fluorescent lifetime detection, for example, has been employed for capillary electrophoresis in both the time and frequency domains [6]. Fluorescent lifetime is also sensitive to excited-state reactions such as fluorescent resonance energy transfer (FRET) which allow one to detect macromolecular associations labelled by two different fluorophores [7]. For microarrays, FRET can be used to detect *in situ* real-time hybridization kinetics in which both probe and target are fluorophore labelled [8].

In most commercial time-resolved systems, time-correlated single photon counting (TCSPC) [9] is employed with PMT detectors. In this case, sensitivity is limited by dark count, which may typically be 400 Hz. Assuming a peak quantum efficiency of (typically) 25%, this corresponds to a detection limit of approximately  $2 \times 10^5 \text{ photons/cm}^2 \text{ s} = 5 \times 10^{-7} \text{ lux}$  for a signal-to-noise ratio (SNR) of 20 dB. For effective lifetime measurement, a detection limit of at least ten times this can be expected. Time resolution (as determined by the full-width at half-maximum (FWHM) of the impulse response of the detector) is limited by jitter in the PMT and instrumentation and can be less than 50 ps. Response of the fluorophore is characterized by absorption cross section and quantum yield; typical fluorophores have cross sections between  $2 \times 10^{-17} \text{ cm}^2$  and  $8 \times 10^{-16} \text{ cm}^2$  (corresponding to molar extinction coefficients between  $\epsilon = 50\,000 \text{ cm}^{-1} \text{ M}^{-1}$  and  $200\,000 \text{ cm}^{-1} \text{ M}^{-1}$ ) and quantum yields ( $\eta$ ) of between 0.05 and 1.0. Assuming  $\eta = 0.5$  and  $\epsilon = 50\,000 \text{ cm}^{-1} \text{ M}^{-1}$ , under steady-state illumination, a detection limit of  $2 \times 10^6 \text{ photons/cm}^2 \text{ s}$  would correspond to surface detection limits down to  $2 \times 10^2 \text{ molecules/cm}^2$  with excitation power of  $10^{20} \text{ photons/cm}^2 \text{ s}$ ; detection limits this low are said to characterize “single-molecule detection capabilities.” Actual detection limits are usually several orders of magnitude greater than this and are limited by background. This background is determined by the effectiveness of optical filtering in removing the excitation wavelength and stray fluorescence. Lower excitation power also results in higher detection limits.

In this paper, we describe the design and measurement of an active CMOS biosensor array for fluorescent-based assays which enables time-gated, time-resolved fluorescence

Manuscript received July 21, 2005; revised June 30, 2006. This work was supported in part by the National Institutes of Health under Grant HG003089 and by the National Science Foundation under Grant BES-0428544.

G. Patounakis and K. L. Shepard are with the Columbia Integrated Systems Laboratory, Department of Electrical Engineering, Columbia University, New York, NY 10027 USA (e-mail: gpat@cisl.columbia.edu; shepard@cisl.columbia.edu).

R. Levicky is with the Department of Chemical Engineering, Columbia University, New York, NY 10027 USA (e-mail: r1268@columbia.edu).

Digital Object Identifier 10.1109/JSSC.2006.883316

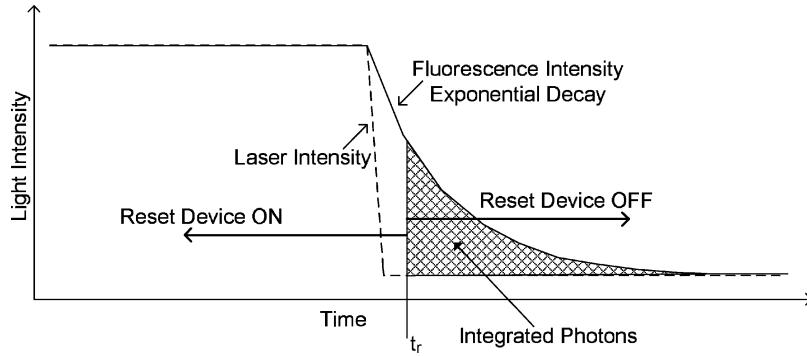


Fig. 1. Time-resolved, time-gated fluorescence detection by integrating photocurrent response.

spectroscopy improving background rejection beyond what is achievable with optical filtering alone [10]. The chip is designed to be sensitive to the lowest probe densities typical of microarray applications ( $10^8$  molecules/cm<sup>2</sup>) with a conventional n-well/p-subphotodiode. Probes are immobilized *directly* on the chip surface, eliminating losses in large, complex optics and allowing for efficient solid-angle collection. Time-gated operation allows for effective elimination of background excitation light. In addition, the ability to distinguish fluorophore lifetime offers the potential to detect the presence of two different fluorophores without the need for multiple optical filters.

In Section II, we describe the principles of time-resolved fluorescent detection. Section III provides a detailed description of the specialized CMOS imager design, while a noise analysis of the chip is presented in Section IV to quantify sensitivity limits. Detailed measurement results are presented in Section IV, and Section VI concludes.

## II. TIME-RESOLVED FLUORESCENCE DETECTION IN CMOS

Most time-resolved fluorescence systems rely on real-time photodetection with a PMT or an APD, which provide high gain and high light sensitivity [11]. Photodiodes, which are the photosensitive devices compatible with a CMOS process, do not have gain and require averaging (in the form of integrating photocurrent onto a capacitor and averaging the results of multiple measurements) to achieve high signal-to-noise performance. Recent work has demonstrated the high sensitivity that photodiode-based CMOS imagers can achieve when long integration times are combined with averaging [12].

In our system, we achieve high sensitivity in what is tantamount to a real-time detection application in which the *transient* fluorescent decay response is extracted, as shown in Fig. 1, following the rapid turn-off of a laser excitation. Time-gating improves the signal-to-background ratio (SBR) of the detector by ensuring that the excitation source is off before collecting the photodiode response. The transient response is repeated (subsampling); each time the integral of the photodiode current ( $i_{\text{det}}(t)$ ) is taken from a different starting time  $t_r$  relative to the laser turn-off time, as shown in Fig. 1, yielding output  $\int_{t_r}^{\infty} i_{\text{det}}(t)dt$ . Subsampling preserves the sensitivity benefits of averaging (by integrating the photocurrent response) and reduces the bandwidth requirements on circuit components since the interval between repeated measurements can be used for data conversion, potentially overlapping with the integration

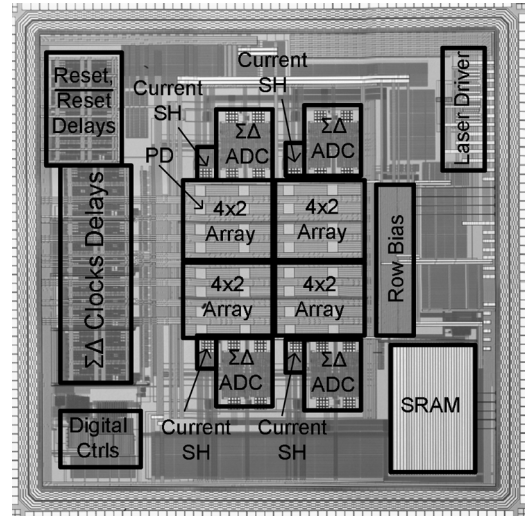


Fig. 2. Die photograph of CMOS sensor chip.

of the next measurement. The result for a single  $t_r$  can also be repeated to improve the overall detection sensitivity. The  $i_{\text{det}}(t)$  transient, which is directly proportional to the instantaneous fluorescence, can be reconstructed by numerical differentiation.

## III. SYSTEM DESCRIPTION

The die photograph of the  $5\text{ mm} \times 5\text{ mm}$  sensor chip as fabricated in a standard mixed-signal  $0.25\text{-}\mu\text{m}$  process is shown in Fig. 2. The  $8 \times 4$  pixel array is time-multiplexed into four current-mode  $\Sigma\Delta$  analog-to-digital converters (ADCs). Digital results are stored in an on-chip SRAM. The arrival time of the reset signal to the pixels ( $t_r$ ) is programmably skewed from the timing of the on-chip laser drivers. An on-chip digital controller, configured externally with a serial bit stream, generates the clocks and control signals for the ADC, steps through the appropriate  $t_r$  values, controls the storage of digital samples, and determines the laser pulse duration.

### A. Pixel Design

The pixel array is divided into four banks of eight pixels with a  $\Sigma\Delta$  ADC for each bank. Each pixel, as shown in Fig. 3, contains two reset transistors ( $M1$  and  $M2$ ), an isolation device ( $M3$ ), a storage capacitor ( $M4$ ), a transconductor ( $M5$ – $M7$ ), and an n-well/p-subphotodiode ( $D1$ ). Each photodiode contains an nwell guard ring to collect carriers generated by

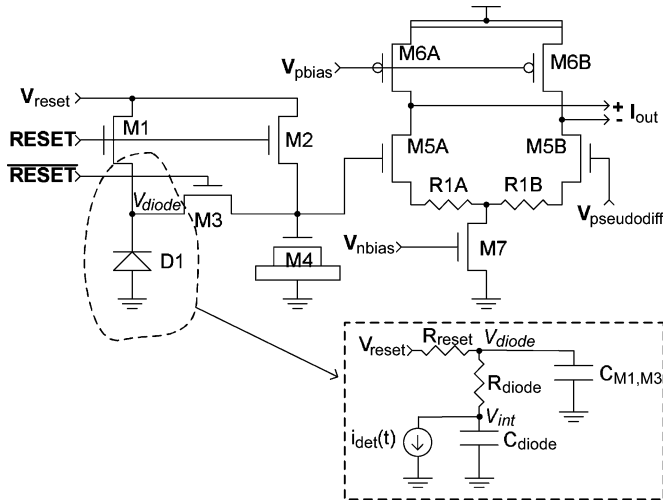


Fig. 3. Pixel schematic. Inset: Equivalent circuit for pixel front-end during reset phase.

neighboring pixels.  $R1A$  and  $R1B$  are nonsilicided polysilicon resistors which linearize the transconductor through source degeneration. The transconductor converts the voltage across the storage capacitor, which results from the integrated photocurrent, into a differential current for subsequent current-mode data conversion.

**Photodiode and Charge Integration in the Pixel:** During the reset phase, as determined by a high value on the *RESET* signal, transistor  $M3$  is off, isolating  $M4$  from  $D1$ , reducing the capacitance on node  $V_{diode}$  to  $C_{pixel}$ , the sum of the reverse-biased capacitance of  $D1$  ( $C_{diode} \cong 0.9$  pF) and the capacitances of  $M1$  and  $M3$  ( $C_{M1,M3} \cong 10$  pF),  $C_{pixel} = C_{diode} + C_{M1,M3}$ . The  $0.5\text{-}\mu\text{m}$   $M1$  reset device is  $3\text{ mm}$  wide to provide a triode region resistance of  $R_{reset} \cong 1.8\ \Omega$ , which allows  $V_{diode}$  to be held within  $20\text{ mV}$  of  $V_{reset}$  even for photodiode currents as large as  $10\text{ mA}$ , which is the photocurrent associated with a  $500\text{ W/m}^2$   $635\text{-nm}$  laser. The isolate transistor  $M3$ , also  $0.5\ \mu\text{m}$  long, is  $1.5\text{ mm}$  wide and acts to mitigate some of the voltage offset associated with charge injection from  $M1$ . The inset of Fig. 3 shows the equivalent circuit of the pixel in the reset phase.  $R_{diode} \cong 1\text{ k}\Omega$  is the parasitic resistance associated with the n-well-bulk connection to the diode and is unfortunately larger than desired because of inadequate placement of contacts to the nwell in the layout. We expect that a more careful design could reduce this resistance to  $200\ \Omega$ . The large value of  $R_{diode}$  limits the maximum sustainable photocurrent to about  $1\text{ mA}$  before blooming occurs in the diode (i.e., the diode becomes forward biased by virtue of the voltage drop across  $R_{diode}$ ). The pixel circuit has two time constants,  $\tau_{diode} = (R_{diode} + R_{reset})C_{diode} \cong 900\text{ ps}$  and  $\tau_{M1,M3} = R_{reset}C_{M1,M3} \cong 20\text{ ps}$ ; the former dominates because of the large value of  $R_{diode}$ . The bandwidth-critical response of the pixel determined by these time constants is how quickly the internal diode voltage across  $C_{diode}$  ( $V_{int}$ ) can track the external diode voltage  $V_{diode}$  during the reset phase. The laser diode pulse fall-time should be greater than both of these time constants for the pixel to track the photocurrent up to  $t_r$ . Transistor  $M3$  acts to provide a larger capacitance for charge integration

( $50\text{ pF}$  when reset is low) while removing the bulk of this capacitance (that of transistor  $M4$ ) from the performance-limiting time constants.

The impulse response of the photodiode sensor,  $h_{det}(t)$ , when convolved with the fluorophore's response to the excitation source (laser diode),  $i_{em}(t)$ , determines the signal output by the detector,  $i_{det}(t)$ :

$$i_{det}(t) = \int_{-\infty}^{\infty} h_{det}(t-t')i_{em}(t')dt'. \quad (1)$$

Therefore, the pixel time constants and the fluorophore lifetime are reflected in  $i_{det}(t)$ . To be easily determinable, fluorophore lifetimes must be greater than the time constants associated with  $h_{det}(t)$ . To calculate an expression for  $h_{det}(t)$  for the pixel, we take  $i_{em}(t) = Q_o\delta(t)$ . The system of differential equations describing the pixel dynamics is then given by

$$\begin{aligned} C_{diode} \frac{dv_{int}}{dt} + \frac{v_{int} - v_{diode}}{R_{diode}} - Q_o\delta(t) &= 0 \\ C_{M1,M3} \frac{dv_{diode}}{dt} + \frac{v_{diode} - v_{int}}{R_{diode}} + \frac{v_{diode} - V_{reset}}{R_{reset}} &= 0. \end{aligned} \quad (2)$$

If one assumes that  $\tau_{M1,M3}/\tau_{diode} \ll 1$  for  $t < t_r$  and  $\tau_{M1,M3}/\tau_{diode} \gg 1$  for  $t > t_r$ , then one finds for  $t < t_r$  that

$$v_{int}(t) = V_{reset} - \frac{Q_o}{C_{diode}} e^{-t/R_{diode}C_{diode}} \quad (3)$$

with  $v_{diode}(t) = V_{reset}$ . Equation (3) makes explicit that the pixel response time limits the ability of  $v_{diode}$  to track  $v_{int}$ . Using these expressions to determine  $v_{int}(t_r)$  and  $v_{diode}(t_r)$  and using these as initial conditions for the solution of (2) for  $t > t_r$ , one finds

$$\begin{aligned} v_{diode}(t) &= V_{reset} + \frac{Q_o}{C_{diode} + C_{M1,M3}} e^{-\frac{t_r}{C_{diode}R_{diode}}} \\ &\quad - \frac{Q_o}{C_{diode} + C_{M1,M3}} e^{-\frac{t_r}{C_{M1,M3}R_{diode}}} \\ &\quad \times e^{-t\left(\frac{C_{M1,M3} + C_{diode}}{C_{M1,M3}C_{diode}R_{diode}}\right)}. \end{aligned} \quad (4)$$

Taking the limit as  $t \rightarrow \infty$  of (4) yields the expression

$$\tilde{v}_{diode}(t_r) = \frac{Q_o}{C_{M1,M3} + C_{diode}} e^{-t_r/R_{diode}C_{diode}} \quad (5)$$

which is the total integrated voltage subsequently sensed by the pixel transconductor. The actual impulse response  $h_{det}(t)$  is proportional to the derivative of  $\tilde{v}_{diode}(t_r)$  with respect to  $t_r$

$$\begin{aligned} h_{det}(t) &\cong -\frac{C_{pixtotal}}{Q_o} \frac{\partial \tilde{v}_{diode}(t)}{\partial t} \\ &= \frac{1}{R_{diode}C_{diode}} e^{-t/R_{diode}C_{diode}}. \end{aligned} \quad (6)$$

**Pixel-Level Transconductor:** The pixel transconductor (see Fig. 3) converts  $V_{diode}$  to a differential current for subsequent current-mode data conversion. When used in this pseudodifferential manner, the transconductance is approximately

$$g_{m,pixel} \approx \frac{-1}{\frac{2}{g_{m5}} + R_{1a}} \quad (7)$$

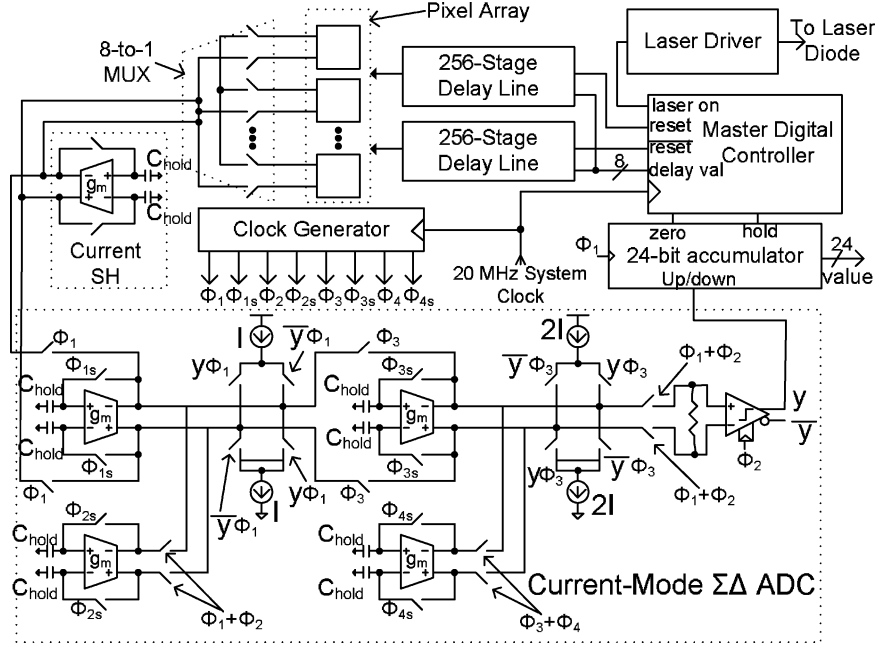


Fig. 4. Simplified top-level system schematic.

where  $g_{m5}$  is the transconductance of transistor M5. In our design,  $R_{1A} = R_{1B} = 500 \Omega$ , yielding a measured transconductance of 0.22 mS. The simulated 3-dB bandwidth is approximately 2.6 MHz. Large input nFETs (4.32 mm/1  $\mu\text{m}$ ), transistors M5A and M5B, are used to reduce  $1/f$  noise and improve matching performance. This, along with the large reset devices, limits the fill factor to approximately 13%. The overall gain of the pixel is  $7.04 \times 10^{-7} \mu\text{A}$  per integrated electron from the photodiode.

### B. Current-Mode Analog-to-Digital Conversion

As shown in Fig. 4, eight differential pixel signal currents are time-multiplexed onto a single current-mode sample-and-hold (SH) element (current copier) consisting of a differential transconductor with two feedback storage capacitors [13]. This SH, therefore, samples  $g_{m,\text{pixel}} \tilde{v}_{\text{diode}}(t)$  for one of the multiplexed pixels. The output of this current-mode SH element is continuously sampled by the  $\Sigma\Delta$  ADC. Using a sampled version of the pixel current rather than feeding the pixel current directly into the ADC prevents charge-injection and clock-feedthrough noise from coupling back into the pixel array through the multiplexer.

The current-mode  $\Sigma\Delta$  ADC, as shown in Fig. 4, is a fully differential second-order 1-bit system [14] with a full-scale input level of  $\pm 10 \mu\text{A}$ . The ADC, therefore, delivers a gain of 205 DN per  $\mu\text{A}$  of pixel current. The differential one-bit current-output DACs are comprised of two cascode current sources and a switch network as shown in Fig. 4. Pattern-dependent supply loading is mitigated with the current-switch design because there is always a fixed current ( $I = 10 \mu\text{A}$ ) flowing through each DAC.

Fig. 5 shows a simplified schematic of the transconductor used in both the current-mode SH element and in the  $\Sigma\Delta$  ADC. This transconductor is based on the design found in

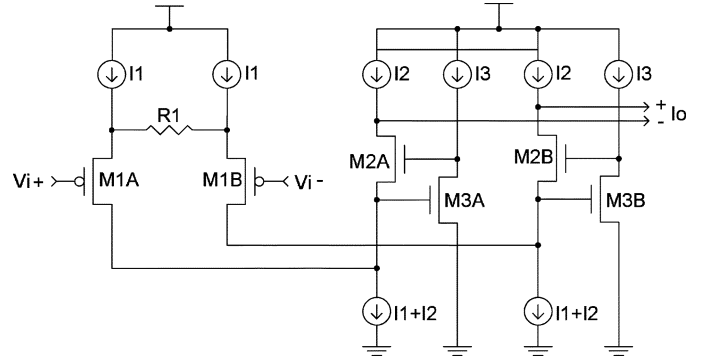


Fig. 5. Simplified transconductor schematic for current copier and  $\Sigma\Delta$ .

[14] but includes a degeneration resistor  $R1$  for linearization and devices  $M3A/M3B$  as an active cascode [15]. For clarity, the schematic does not include the triode region common-mode feedback devices detailed in [14] for properly setting the common-mode level when the transconductor is used with fully differential feedback. The DC transconductance ( $g_m = I_o/(V_i^+ - V_i^-) \approx 0.2 \text{ mS}$ ) is approximately 0.1 mS. The closed-loop bandwidth is given by  $(g_m/2\pi(C_{\text{hold}}/2)) (\approx 120 \text{ MHz})$ , where  $C_{\text{hold}} (\approx 58 \text{ pF})$  is the holding capacitance, implemented as inversion-mode MOS capacitors. This bandwidth allows over 12 bit of settling accuracy to be achieved with four-phase nonoverlapping clocks operating with an 8- $\mu\text{s}$  period.

The active cascode devices in the output stage of the transconductor increase the performance of the circuit by mitigating the effects of finite device output conductance. The differential pair sees a very low input impedance ( $R_i$ ) looking into the active cascode comprised of transistors M2 and M3

$$R_i = \frac{r_{o2} + R_L/2}{1 + g_{m2}r_{o2} + g_{m2}g_{m3}r_{o2}r_{o3}}. \quad (8)$$

The expression assumes a differential load resistance of  $R_L$  loading the transconductor output and that the pMOS current sources have a high output resistance compared to the differential load. This *low* input resistance looking into the active cascode allows the majority of the current switched by the differential input pair to flow to the output instead of being shunted by the output conductance of the current source  $I_1 + I_2$ . The active cascode also boosts the output impedance ( $R_o$ ) of the transconductor

$$R_o = [r_{o2} + r_{eq} + g_{m2}r_{o2}r_{eq} + g_{m2}g_{m3}r_{o2}r_{o3}r_{eq}]||r_{oI2} \quad (9)$$

where  $r_{eq}$  is the parallel combination of the nMOS current source and impedance looking into the differential pair device  $M1$  and  $r_{oI2}$  is the output resistance of current source  $I_2$ . In this case, the *larger* the output impedance of the transconductor, the less significant the loading effects of the next stage become.

The one-bit  $\Sigma\Delta$  output is used as an “up” or “down” signal for a 24-bit accumulator, which is a simple low-pass digital filter. The 12-bit value generated by the accumulator after running the  $\Sigma\Delta$  for 4096 cycles has a relative accuracy of approximately 11 b, limited by idle tones in the  $\Sigma\Delta$ . The measured detrimental effect of idle tones is less than what behavioral modeling of the ADC predicts because of the dithering effect of noise at the input of the ADC from the current-copier SH and other analog noise sources in the  $\Sigma\Delta$  loop [16].

Accumulator results are cached into on-chip SRAMs, which eliminates the need for firing noisy off-chip drivers during repeated measurements. The outputs of the four accumulators are fed to the input of the SRAM controller that coordinates writing these to a single  $2048 \times 24$  array. The address space of the SRAM is organized by  $\Sigma\Delta$  subblocks and by which pixel within the subblock is being written. The SRAM can be written in a “single-pixel” mode for a maximum of 2048 24-b pixel values or in a “multiple-pixel” mode in which 64 values for each of the 32 pixels are stored. When measurements are complete, the entire contents of the SRAM can be loaded off-chip in under  $310 \mu s$ .

A single measurement takes 4097 ADC cycles to complete; one additional cycle is consumed to allow the SH to settle. This means that one measurement on each of four pixels can be repeated every 33 ms.

### C. Reset and Laser-Diode-Driver Control

The chip must drive both the array reset signal and the off-chip laser with the ability to vary the skew between these signals to achieve the time-resolved fluorescence detection shown in Fig. 1.

The laser driver consists of a variable-width inverter with independent tunability of the pull-up and pull-down widths, selected digitally with two 7-bit control words. To accommodate laser diodes with operating voltages greater than 2.5 V, thick oxide 3.3-V I/O are used in the laser driver output circuitry. This also allows the diode to tolerate overshoot at the near-end, which sometimes occurs as a result of reflections against the highly nonlinear load resistance turn-on characteristic of the laser diode. The maximum current sourcing capability at 2.7-V

TABLE I  
SIMULATED READ NOISE SUMMARY

Item	Input Referred Noise
Reset noise ( $\overline{V_{n,reset}^2}$ )	$6.776 \times 10^{-11} V^2$
Pixel transconductor noise ( $\overline{V_{n,pixgm}^2}$ )	$2.915 \times 10^{-10} V^2$
Current-mode SH noise ( $\overline{V_{n,currsh}^2}$ )	$2.046 \times 10^{-9} V^2$
Quantization noise ( $\overline{V_{n,quant}^2}$ )	$4.930 \times 10^{-10} V^2$
Total	$2.898 \times 10^{-9} V^2$ ( $3.74 \times 10^8 \frac{photons}{cm^2}$ )

output is greater than 130 mA, which is sufficient to drive commercial laser diodes with 50 mW of optical output. Larger laser diodes with input capacitances of up to 40 pF can be driven by up to four off-chip 50- $\Omega$  transmission lines in parallel. Near-end fall times of about 500 ps are achieved. Pulse width and synchronization are determined by the master digital controller. Pulse width can be varied in 50-ns intervals up to  $204.8 \mu s$ , but typically a pulsewidth of 300 ns is used.

A programmable, variable delay line is used to trigger the pixel reset predrivers. This delay can be multiples of  $T_{cycle} = 50$  ns (the period of the 20 MHz system clock) combined with subclock-period delay generation with a simple 256-stage inverter chain delay line (with stage delay,  $T_{delay} \cong 230$  ps) as shown in Fig. 4:  $t_r = nT_{cycle} + mT_{delay}$ , where  $m$  and  $n$  are positive integers. An eight-bit multiplexer is used to choose one of the phases of the delay line. The delay line and multiplexer are carefully laid out to limit mismatch between buffer stages due to layout parasitics.

Because large on-chip drivers for the reset and laser diode drivers are rapidly switching to achieve sufficient resolution for time-resolved detection, power-supply and substrate noise issues are a concern for the sensitive analog circuits of the array and ADC. The slew rate of the reset signal is limited to slightly less than 1 ns to control noise generation. The pixel array and  $\Sigma\Delta$  ADC are isolated by a double guard ring. Supplies are carefully separated and decoupled on-chip. All bias currents and voltages are fed in from one side of the chip while all digital signals interface from the other side.

## IV. NOISE ANALYSIS OF INTEGRATED SIGNAL

Circuit read noise and photon shot noise determine the SNR and the dynamic range for measurement of  $\tilde{v}_{diode}(t)$ . The read noise consists of four major components: the pixel reset noise, the pixel transconductor noise, the current-mode SH noise, and the quantization noise of the ADC. Averaging of repeated measurements can be used to reduce the first three read noise sources and leave the system noise floor determined by the quantization limit of the ADC.

### A. Read Noise

Simulated read noise sources are summarized in Table I.

*Pixel Reset Noise:* As shown in Fig. 3, there are two capacitors that are reset during the reset phase,  $C_{pixel} = C_{diode} + C_{M1,M3} \approx 10.9$  pF and the sampling capacitance  $C_{M4}$  ( $\approx 30$  pF), which is determined by the gate capacitance of M4. The system is assumed to be in steady-state

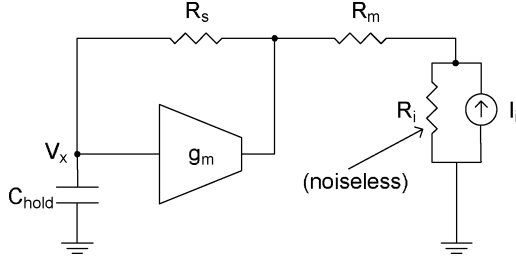


Fig. 6. Half circuit for current-mode SH sampled noise analysis.

because of the long reset times employed; therefore, the sampled noise voltage power on a capacitor  $C$  is given by  $kT/C$ .<sup>1</sup> The total mean-squared noise charge is given by

$$\overline{Q_{n,\text{reset}}^2} = \frac{kT}{C_1} C_1^2 + \frac{kT}{C_{M4}} C_{M4}^2 (= 1.694 \times 10^{-31} \text{C}^2 \text{ at } 300 \text{ K}). \quad (10)$$

After reset, the switch M3 is turned on while switches M1 and M2 are turned off. Therefore, the effective capacitance of the input node to the pixel transconductor is given by  $C_{\text{pixtotal}} = C_{\text{pixel}} + C_{M4}$  ( $\approx 50$  pF with the additional capacitance of the switch M3). Consequently, the mean squared noise voltage at the input of the transconductor due to the reset devices is given by

$$\overline{V_{n,\text{reset}}^2} = \frac{\overline{Q_{n,\text{reset}}^2}}{C_{\text{pixtotal}}^2} (= 6.776 \times 10^{-11} \text{V}^2 \text{ at } 300 \text{ K}). \quad (11)$$

**Pixel Transconductor Noise:** Referring to Fig. 3, the pixel transconductor noise is dominated by the thermal noise of the degeneration resistor and the channel thermal noise of transistors M5 and M6. The drain current noise power spectral density (PSD) of transistor M5 is given by

$$S_{n,M5} = 2qI_{DS5} \left( 1 + e^{-\frac{qV_{DS5}}{kT}} \right) + \frac{K_{M5}}{C_{ox}W_{M5}L_{M5}} \frac{g_{M5}^2}{f} \quad (12)$$

where  $K_{M5}$  is the  $1/f$  noise constant for M5 and  $I_{DS5}$  is the drain-to-source current of M5. Transistor M5 is biased in moderate inversion but close enough to weak inversion to justify the use of weak-inversion expressions for noise analysis. Similarly, the drain current noise PSD of transistor M6 is given by

$$S_{n,M6} = 4kT \frac{2}{3} g_{M6} + \frac{K_{M6}}{C_{ox}W_{M6}L_{M6}} \frac{g_{M6}^2}{f}. \quad (13)$$

Transistor M6 is biased near strong inversion so the strong inversion noise expression is used. Finally, the resistor current noise PSD of degeneration resistor  $R_1$  is given by

$$S_{n,R1} = \frac{4kT}{R_1}. \quad (14)$$

Using these expressions in simulation, we find a total integrated input referred noise power of  $2.915 \times 10^{-10} \text{V}^2$ . The  $1/f$  noise sources of the pixel transconductor represent approximately 10% of the total noise over the integrated bandwidth.

**SH Noise:** Additional noise is associated with sampling the current on the current-mode SH. Fig. 6 shows the half circuit

used for this analysis. In this case, we seek the noise voltage stored on node  $V_x$ .  $R_i$  is the output resistance (the noise of which is neglected) of the driving stage (pixel transconductor), modeled by the current source  $I_i$ . Resistors  $R_m$  and  $R_s$  are the analog multiplexor switch on-resistance and current-mode SH feedback switch on-resistance, respectively. The transconductor is modeled as an ideal transconductor with transconductance  $g_m$  and output resistance  $r_o$ . For large  $R_i$ , the sampled noise voltage on  $V_x$  is dominated by the noise of  $R_s$  and the transconductor equivalent output noise current. Assuming  $r_o \gg R_s$ , and  $g_m r_o \gg 1$ , the total integrated noise sampled on  $V_x$  from the switch resistance  $R_s$  is given by

$$\overline{V_{n,Rs}^2} \approx 2 \times \frac{kTR_s}{g_m r_o^2 C_{\text{hold}}}. \quad (15)$$

This noise decreases as both the transconductance and holding capacitance of the current-mode SH increase. For large  $r_o$ , the total integrated noise due to the equivalent single-ended transconductor output current noise power spectral density  $S_{n,gm}$  is given by

$$\overline{V_{n,gm}^2} \approx 2 \times \frac{S_{n,gm}}{g_m C_{\text{hold}}}. \quad (16)$$

Once again, the circuit becomes less noisy when both the transconductance and holding capacitance increase. The total sampled noise on  $V_x$ , given by  $\overline{V_{n,gm}^2} + \overline{V_{n,Rs}^2}$ , when input-referred to  $v_{\text{diode}}$  is denoted as  $\overline{V_{n,\text{currsh}}^2}$  in Table I. This noise,  $2.046 \times 10^{-9} \text{V}^2$ , constitutes more than two thirds of the total read noise of the sensor.

**Quantization Noise:** The equivalent quantization noise ( $\overline{V_{n,\text{quant}}^2}$ ) referred back to the pixel  $v_{\text{diode}}$  node is  $4.930 \times 10^{-10} \text{V}^2$ , assuming 12-bit data conversion and a 30-mV swing on  $\tilde{v}_{\text{diode}}(t)$ .

The total rms read noise is  $54 \mu\text{V}$ , which corresponds to approximately  $3.74 \times 10^8$  photons/cm<sup>2</sup> for a quantum efficiency of 45% and a  $C_{\text{pixtotal}}$  capacitance of 50 pF.

### B. Photon Shot Noise Analysis

Unlike the shot noise analysis that is traditionally applied to imagers, the time-varying light intensity resulting from the fluorophore decay produces nonstationary shot noise statistics. The mean-square shot noise charge is given by [18], [19]

$$\overline{Q_{n,\text{sh}}^2} = \int_{t_r}^{\infty} q i_{\text{em}}(t) dt. \quad (17)$$

Consistent with previous analyses, if we take the fluorophore's response to be a monoexponential decay represented by  $i_{\text{em}}(t) = I_o e^{-t/\tau_{\text{fluor}}}$ , where  $\tau_{\text{fluor}}$  is the fluorophore's lifetime and  $I_o$  is the initial intensity of the fluorescence decay, the integrated shot noise is given by

$$\overline{Q_{n,\text{sh}}^2} = q\tau_{\text{fluor}} I_o e^{-t_r/\tau_{\text{fluor}}} \quad (18)$$

yielding an input-referred mean-square voltage noise of  $\overline{V_{n,\text{sh}}^2} = (\overline{Q_{n,\text{sh}}^2}/C_{\text{pixtotal}}^2)$ . Since the signal power is proportional to  $e^{-2t_r/\tau}$ , the SNR in the shot-noise-limited regime decreases with increasing  $t_r$  as  $e^{-t_r/\tau}$ .

<sup>1</sup>This assumption of "long" reset time is not the case in most APS imagers and  $kT/C$  overestimates the actual sampled noise voltage power [17].

### C. Time-Gated Background Rejection

The time-gated behavior of the sensor provides for background rejection of the excitation source, even in the absence of optical filtering. The background excitation reaching the sensor is assumed to have an exponential decay time given by  $\tau_{\text{diode}}$ , which is valid if  $\tau_{\text{diode}}$  is much larger than the laser turn-off time. Furthermore, fluorophores excited during the turn-off transient are neglected so that the fluorescent signal is characterized by a decay time given by the fluorescent lifetime  $\tau_{\text{fluor}}$ , which is valid if  $\tau_{\text{fluor}} \gg \tau_{\text{diode}}$ .<sup>2</sup> Let  $Q_{\text{total}}$  be the total charge generated in the sensor due to the pulsed excitation source in the absence of fluorophores. When the fluorophores are present, they absorb a fraction of the photons given by  $\sigma c_{\text{surface}}$ , where  $\sigma$  is the absorption cross section and  $c_{\text{surface}}$  is the surface concentration of fluorophores. The instantaneous currents generated in the sensor due to the excitation source (background) and the fluorophores (signal) are given by

$$I_{\text{background}}(t) = \frac{(1 - \sigma c_{\text{surface}})Q_{\text{total}}}{\tau_{\text{diode}}} e^{-t/\tau_{\text{diode}}} \quad (19)$$

$$I_{\text{signal}}(t) = \frac{\eta \sigma c_{\text{surface}}}{\tau_{\text{fluor}}} e^{-t/\tau_{\text{fluor}}} \quad (20)$$

where  $\eta$  is the quantum yield of the dye.

The signal-to-background ratio is then given by

$$\begin{aligned} \text{SBR} &= \frac{\int_{t_r}^{\infty} I_{\text{background}}(t) dt}{\int_{t_r}^{\infty} I_{\text{signal}}(t) dt} \\ &= \frac{\sigma c_{\text{surface}} \eta}{1 - \sigma c_{\text{surface}}} e^{-t_r \frac{\tau_{\text{diode}} - \tau_{\text{fluor}}}{\tau_{\text{diode}} \tau_{\text{fluor}}}}. \end{aligned} \quad (21)$$

Expressing this in decibels yields

$$\begin{aligned} \text{SBR}_{\text{dB}} &= t_r \frac{20}{\ln(10)} \frac{\tau_{\text{diode}} - \tau}{\tau_{\text{diode}} \tau} \tau_{\text{diode}} \tau \\ &\quad + 20 \log_{10} \left( \frac{\sigma c_{\text{surface}} \eta}{1 - \sigma c_{\text{surface}}} \right). \end{aligned} \quad (22)$$

$\text{SBR}_{\text{dB}}$  increases linearly with  $t_r$ , while, as described in Section IV-C, the SNR decreases with increasing  $t_r$ . An optimal value of  $t_r$  for detection occurs when the SNR equals the SBR.

## V. RESULTS

Here, we present the experimental results quantifying the quantum efficiency, SNR performance, dynamic range (DR), and time-domain response of the sensor chip. A summary of the measured performance of the chip is presented in Table II.

### A. Quantum Efficiency

Fig. 7 presents the measured external quantum efficiency of the nwell/p-subphotodiode using a fairly standard measurement setup including a monochromator, integrating sphere, and calibrated photodetector. Peak quantum efficiencies in the range of 0.45–0.5  $e^-/ph$  occur at wavelengths between 600–700 nm for the relatively deep diode junctions, suggesting peak per-

<sup>2</sup>In general, the actual fluorescent signal will be given by the convolution integral of (1). Deconvolution techniques can be used to determine  $\tau_{\text{fluor}}$  even when  $\tau_{\text{diode}}$  is comparable [20].

TABLE II  
CHIP SPECIFICATIONS AND MEASURED PERFORMANCE

Item	Value
<b>Chip</b>	
Technology	TSMC 0.25 $\mu\text{m}$
	Mixed-Signal CMOS
Die Size	5 mm $\times$ 5 mm
Clock Speed	20 MHz
SRAM Size	2048x24-bits
Sensitivity	$1.15 \times 10^8$ photons/cm <sup>2</sup>
Linearity	9 bits (w/o calibration)
Delay line resolution	230 ps
Laser drive maximum current (at 2.7 V)	130 mA
Time to complete single measurement	33 ms
<b>Pixel array</b>	
Array size	8 $\times$ 4
Quantum efficiency (at 635 nm)	0.45
Pixel size	180 $\times$ 415 $\mu\text{m}^2$
Photodiode size	100 $\times$ 100 $\mu\text{m}^2$
Transconductor gain	0.22 mS
Pixel gain	$7.04 \times 10^{-7} \mu\text{A}/e^-$
Dark signal	10.4 $\mu\text{A}/s$
$\tau_{\text{diode}}$	1.2 ns
$R_{\text{diode}}$	1.4 k $\Omega$
<b>ADC</b>	
Architecture	Current Mode $\Sigma\Delta$
Order	2
DAC	1-bit Differential
ADC gain	205 DN/ $\mu\text{A}$
Cycle Time	8 $\mu\text{s}$ (>12-bit settling)
Cycles per Sample	4096 (adjustable)
Input full scale	$\pm 10 \mu\text{A}$

formance for dyes operating in this wavelength range, such as AlexaFluor 633 (with peak absorption at 630 nm). The structure in the curve, particularly evident at the longer wavelengths, is due to interference effects in the dielectric stack.

### B. SNR and DR Characterization

Both the SNR/DR and time-domain characterization are performed with the sensor mounted with the laser diode and focusing optics as shown in Fig. 8. To keep the optics simple, the elliptical shape of the laser beam is not altered. The laser diode used for these measurements is a 635-nm, 5-mW AlGaInP diode packaged in a 9-mm CAN style package. Mounted on a PCB that is positioned over the PCB containing the sensor chip, up to four cables connect the laser to the laser diode drivers on the sensor chip. The biochip sensor is packaged in a ceramic quad-flat-pack package for these measurements.

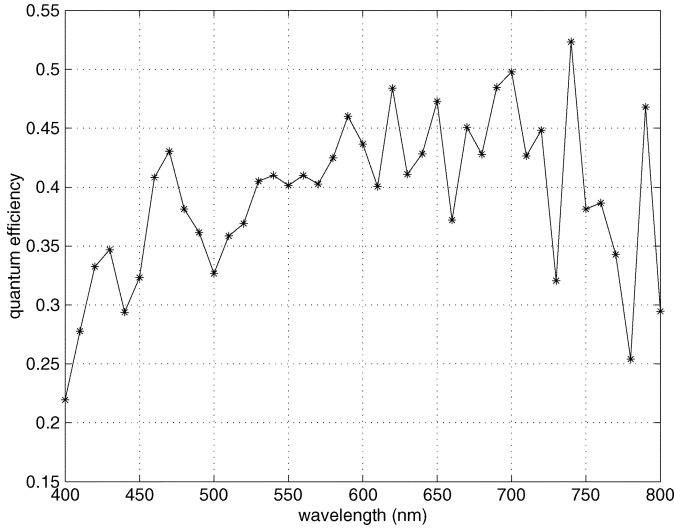


Fig. 7. Quantum efficiency of n-well/p-subphotodiode sensor.

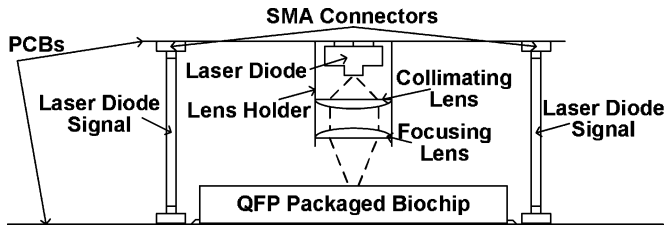


Fig. 8. Packaging of sensor chip with laser and simple focusing optics.

Fig. 9 characterizes the sensor sensitivity. In this case,  $t_r$  is chosen to position the end of the reset phase 8.5 ns before the laser diode turn-off, allowing laser diode power to be directly integrated in the sensor. Neutral density filters are used to vary the laser signal strength. While the neutral density filters have transmission tolerances of only  $\pm 10\%$ , the transmission of individual neutral density filters is calibrated to remove this source of possible measurement error. Each point in the signal curve is the average of 2047 measurements. The signal curve shows good linearity over three orders of magnitude. The integral linearity is limited principally by the in-pixel transconductor to about 9 b. This can be calibrated to further improve linearity, leaving the system to perform at the limit of the ADC (11 b). We note that the illumination is measured in units of photons/cm<sup>2</sup>, since this imager is measuring *integrated* photon flux.

The noise curves of Fig. 9 are generated by taking the average of blocks of  $N$  consecutive measurements in the original 2047 measurement dataset. The standard deviation of the floor( $2047/N$ ) averaged blocks of data is recorded as the noise after averaging. The noise curves show the effect of averaging on reducing the noise floor of the system. Averaging 64 points yields a noise floor close to the 12-b quantization noise limit of the system. At higher integrated photon flux, the noise curves acquire a one-half slope due to photon shot noise. The system shows a peak SNR, limited by photon shot noise, of 64 dB and a dynamic range of 74 dB. The read noise floor of the sensor (without averaging) shown in Fig. 9 ( $5 \times 10^8$  photons/cm<sup>2</sup>) is slightly larger than that predicted

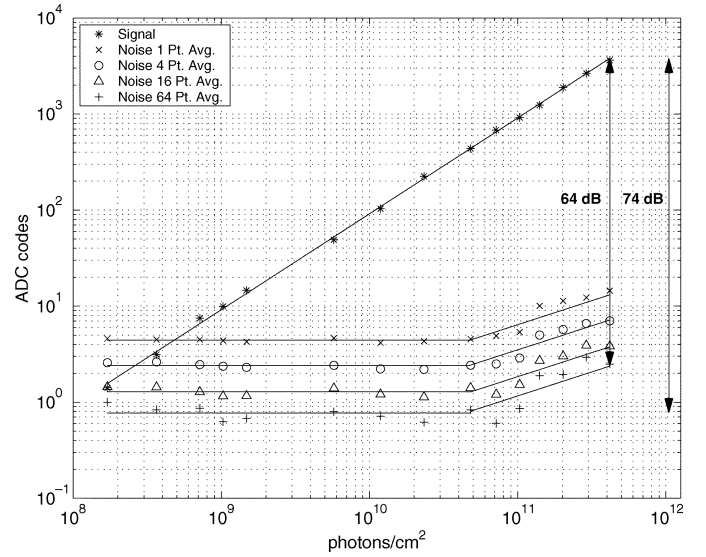


Fig. 9. Complete sensor system sensitivity.

by simulation ( $3.74 \times 10^8$  photons/cm<sup>2</sup>), probably due to slight underestimation of the read noise contribution of the pixel transconductor.

The measured dark current in the photodiode is approximately 2.31 pA, which corresponds to a dark current signal from the pixel transconductor of 10.4  $\mu$ A/s of integration. The corresponding dark current shot-noise level is approximately  $10^{-3}$  digital numbers (DN) for 12-b conversion, which is well below the quantization noise limit.

The results shown in Fig. 9 consider the excitation source (laser diode) the “desired” signal. Therefore, the dynamic range shown in Fig. 9 is the true dynamic range of the sensor. However, in time-gated operation, if the excitation source is not completely “off” at  $t_r$ , the *effective* dynamic range will be reduced because the sensor will saturate at lower fluorescent signal levels.

### C. Time-Domain Characterization

Fig. 10 presents the time-domain response of the sensor in which  $t_r$  is varied to reconstruct the actual turn-off transient of the laser. The solid lines represent the output from a 12-GHz-bandwidth, New Focus 1577-A photodetector as measured by an Agilent 86100B oscilloscope. The circles show the numerically differentiated output of the sensor. The laser fall-time is varied from approximately 1 to 5 ns. For fastest fall times, we find that the sensor output lags the high-speed detector output, due to the limitations of the  $\tau_{\text{diode}}$  time constant described in Section III-A.

To gain more insight into the time-domain response, the impulse response of the system is measured with a PiLas Picosecond Laser Diode System with a 635-nm laser diode head. The laser is capable of producing laser pulses of less than 40-ps FWHM with peak collimated beam power as high as 150 mW. The laser is triggered by the chip’s laser driver output, and the delay from the chip’s laser driver signal to when the laser is actually fired is controlled by varying the



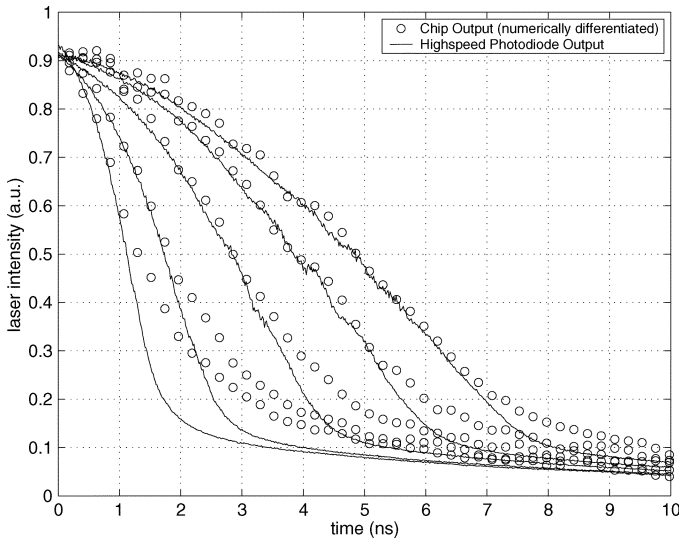


Fig. 10. Time-resolved detection of laser turn-off edge.

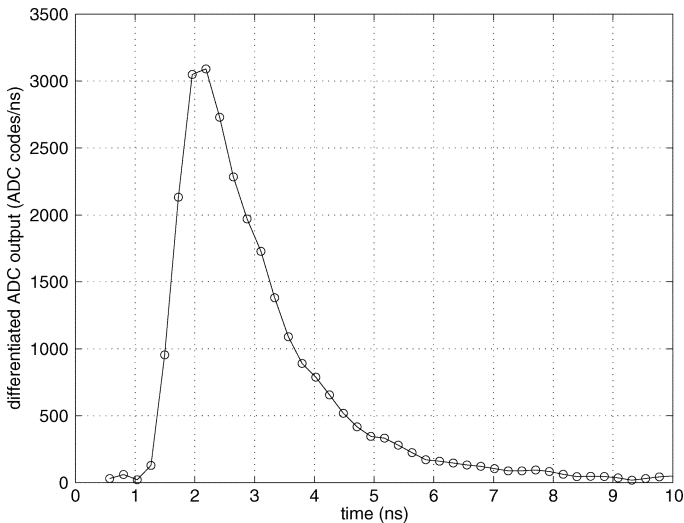


Fig. 11. Differentiated impulse response of system.

coaxial cable length carrying the trigger signal. Fig. 11 shows the numerically differentiated ADC output of the system for an impulse excitation. Each time sample is measured 32 times and subsequently averaged to get the final waveform. The circles depict the numerically differentiated output of the sensor. The system shows an exponential decay as predicted by the discussion of Section III-A. An artifact of the four-point numerical differentiation algorithm [21] is apparent during the beginning of the pulse because the algorithm does not produce accurate results for a signal with such a high frequency edge and effectively low-pass filters it. The exponential decay has a time constant ( $\tau_{\text{diode}}$ ) of 1.2 ns, suggesting a parasitic  $R_{\text{diode}}$  resistance of approximately 1400  $\Omega$ .

For this value of  $\tau_{\text{diode}}$ , even for long-lifetime quantum-dot fluorophores, we find time-gating alone does not provide adequate background rejection for detection. To detect surface concentrations on the order of  $10^8 \text{ cm}^{-2}$ , at least 160 dB of excitation rejection is required, which is unachievable within

the constraints described in Section IV-C. Even if  $\tau_{\text{diode}}$  were reduced through design improvement to 500 ps, time-gating alone would not provide sufficient SBR. As a result, we have added an OD 5 23-layer  $\text{SiO}_2/\text{TiO}_2$  thin-film optical filter to the chip; combined with time gating, more than 160 dB of background rejection is achieved.

## VI. CONCLUSION

We have demonstrated a CMOS fluorescence array sensor with sensitivities of almost  $c_{\text{surface}} = 10^8 \text{ molecules/cm}^2$ , a dynamic range of 74 dB, and subnanosecond timing resolution. This substrate should enable powerful, low-cost devices for surface-based biomolecular assays.

With the optical filter in place, measurements with fluorescent molecules “spotted” directly on the photodiode as well as hybridization experiments with fluorescently tagged DNA and DNA probes are on-going and will be reported in a biology-related journal.

## REFERENCES

- [1] K. U. Mir and E. M. Southern, “Sequence variation in genes and genomic data: Methods for large-scale analysis,” *Annu. Rev. Genom. Human Genetics*, vol. 1, pp. 329–360, Sep. 2000.
- [2] M. F. Templin, D. Stoll, M. Schrenk, P. C. Traub, C. F. Vohringer, and T. O. Joos, “Protein microarray technology,” *Trends Biotechnol.*, vol. 20, pp. 160–166, Apr. 2002.
- [3] M. Schena, R. A. Heller, T. P. Theriault, K. Konrad, E. Lachenmeier, and R. W. Davis, “Microarrays: Biotechnology’s discovery platform for functional genomics,” *Trends Biotechnol.*, vol. 16, pp. 301–306, Jul. 1998.
- [4] J. G. Hacia and F. S. Collins, “Mutational analysis using oligonucleotide microarrays,” *J. Medical Genet.*, pp. 730–736, Oct. 1999.
- [5] X. Michalet, F. F. Pinaud, L. A. Bentolila, J. M. Tsay, S. Doose, J. J. Li, G. Sundaresan, A. M. Wu, S. S. Gambhir, and S. Weiss, “Quantum dots for live cells, *in vivo* imaging, and diagnostics,” *Science*, vol. 307, pp. 538–544, Jan. 2005.
- [6] S. L. McIntosh, B. K. Nunnally, A. R. Nesbit, T. G. Deligeorgiev, N. I. Gadjev, and L. B. McGown, “Fluorescence lifetime for on-the-fly multiplex detection of DNA restriction fragments in capillary electrophoresis,” *Anal. Chem.*, vol. 72, no. 21, pp. 5444–5449, Nov. 2000.
- [7] P. I. H. Bastiaens and A. Squire, “Fluorescence lifetime imaging microscopy: Spatial resolution of biochemical processes in the cell,” *Trends Cell Biology*, vol. 9, pp. 48–52, Feb. 1999.
- [8] R. A. Cardullo, S. Agrawal, C. Flores, P. C. Zamecnik, and D. E. Wolf, “Detection of nucleic acid hybridization by nonradiative fluorescence resonance energy transfer,” *Proc. Nat. Acad. Sci.*, vol. 85, pp. 8790–8794, Dec. 1988.
- [9] D. V. O’Connor and D. Phillips, *Time-Correlated Single Photon Counting*. New York: Academic, 1984.
- [10] G. Patounakis, K. L. Shepard, and R. Levicky, “Active CMOS biochip for time-resolved fluorescence detection,” in *Proc. Symp. VLSI Circuits*, Jun. 2005, pp. 68–71.
- [11] R. A. Yotter and D. M. Wilson, “A review of photodetectors for sensing light-emitting reporters in biological systems,” *IEEE Sensors J.*, vol. 3, no. 3, pp. 288–303, Jun. 2003.
- [12] H. Eltoukhy, K. Salama, A. El Gamal, M. Ronaghi, and R. Davis, “A 0.18  $\mu\text{m}$  CMOS  $10^{-6}$  lux bioluminescence detection system-on-chip,” in *Proc. IEEE Int. Solid-State Circuits Conf.*, Feb. 2004, pp. 222–223.
- [13] S. J. Daubert, D. Vallancourt, and Y. P. Tsividis, “Current copier cells,” *Electron. Lett.*, vol. 24, pp. 1560–1562, Oct. 1988.
- [14] S. J. Daubert and D. Vallancourt, “A transistor-only current-mode  $\Sigma\Delta$  modulator,” *IEEE J. Solid-State Circuits*, vol. 27, no. 5, pp. 821–830, May 1992.
- [15] B. Razavi, *Design of Analog CMOS Integrated Circuits*. New York: McGraw-Hill, 2001.

- [16] D. Hyun and G. Fischer, "Limit cycles and pattern noise in single-stage single-bit delta-sigma modulators," *IEEE Trans. Circuits Syst. I, Fundam. Theory Appl.*, vol. 49, no. 5, pp. 646–656, May 2002.
- [17] H. Tian, B. Fowler, and A. El Gamal, "Analysis of temporal noise in CMOS photodiode active pixel sensor," *IEEE J. Solid-State Circuits*, vol. 36, no. 1, pp. 92–101, Jan. 2001.
- [18] T. M. Niebauer, R. Schilling, K. Danzmann, A. Rudiger, and W. Winkler, "Nonstationary shot noise and its effect on the sensitivity of interferometers," *Phys. Rev. A*, vol. 43, pp. 5022–5029, May 1991.
- [19] B. E. A. Saleh and M. C. Teich, *Fundamentals of Photonics*. New York: Wiley, 1991.
- [20] J. R. Lakowicz, *Principles of Fluorescence Spectroscopy*. Boston, MA: Kluwer/Plenum, 1999.
- [21] J. Nearing, "Mathematical tools for physics," 2003 [Online]. Available: <http://www.physics.miami.edu/nearing/mathmethods>



**George Patounakis** (S'00–M'05) received the B.S. degree from Rutgers University, New Brunswick, NJ, in 2000, and the M.S. and Ph.D. degrees from Columbia University, New York, NY, in 2001 and 2005, respectively, all in electrical engineering. He is currently working toward the M.D. degree at the Robert Wood Johnson Medical School, New Brunswick, NJ.

His research interests include interfacing biosensing with silicon microelectronics, on-chip power management, and high-speed intrachip interconnects.

Dr. Patounakis was the recipient of the Columbia SEAS Presidential Fellowship and an Intel Ph.D. fellowship.

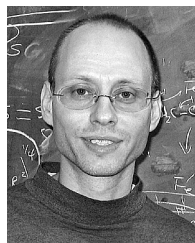


**Kenneth L. Shepard** (S'85–M'92–SM'03) received the B.S.E. degree from Princeton University, Princeton, NJ, in 1987, and the M.S. and Ph.D. degrees in electrical engineering from Stanford University, Stanford, CA, in 1988 and 1992, respectively.

From 1992 to 1997, he was a Research Staff Member and Manager with the VLSI Design Department, IBM T. J. Watson Research Center, Yorktown Heights, NY, where he was responsible for the design methodology for IBM's G4 S/390 microprocessors. Since 1997, he has been with Columbia University,

New York, NY, where he is now an Associate Professor. He also served as Chief Technology Officer of CadMOS Design Technology, San Jose, CA, until its acquisition by Cadence Design Systems in 2001. His current research interests include design tools for advanced CMOS technology, on-chip test and measurement circuitry, low-power design techniques for digital signal processing, low-power intrachip communications, and CMOS imaging applied to biological applications.

Dr. Shepard was the recipient of the Fannie and John Hertz Foundation Doctoral Thesis Prize in 1992. At IBM, he received Research Division Awards in 1995 and 1997. He was also the recipient of the National Science Foundation CAREER Award in 1998 and IBM University Partnership Awards from 1998 through 2002. He was also awarded the 1999 Distinguished Faculty Teaching Award from the Columbia Engineering School Alumni Association. He has been an Associate Editor of the IEEE TRANSACTIONS ON VERY LARGE SCALE INTEGRATION (VLSI) SYSTEMS and was the technical program chair and general chair for the 2002 and 2003 International Conference on Computer Design, respectively. He has served on the program committees for ICCAD, ISCAS, ISQED, GLS-VLSI, TAU, and ICCD.



**Rastislav Levicky** received the B.S. degree from Columbia University, New York, NY, and the Ph.D. degree from the University of Minnesota, Minneapolis, in 1991 and 1996, respectively, both in chemical engineering.

He then spent 18 months as a National Research Council Postdoctoral Associate with the National Institute of Standards and Technology (NIST), Gaithersburg, MD, investigating biological macromolecules at interfaces with focus on understanding the relationship between structure and biological activity of DNA monolayers. In July 1998, he joined the Chemical Engineering faculty at Columbia University as a tenure-track Assistant Professor. His current research interests encompass biologically functional surfaces, polymer thin films and interfaces, and nano-organized biological and synthetic materials.

Dr. Levicky is a member of the American Institute of Chemical Engineers, the American Chemical Society, the American Physical Society, and the Materials Research Society. He was the recipient of the Union Carbide Kenan Analytical Award, the Sigma Xi Outstanding Poster Award, the National Science Foundation's CAREER Award for Young Investigators, and the 2001 Distinguished Faculty Teaching Award from the Columbia Engineering School Alumni Association.